

A brightening of Jupiter's auroral 7.80- μm CH₄ emission during a solar-wind compression

J. A. Sinclair¹, G. S. Orton¹, J. Fernandes^{1,2}, Y. Kasaba³, T. M. Sato⁴, T. Fujiyoshi⁵, C. Tao⁶, M. F. Vogt⁷, D. Grodent⁸, B. Bonfond⁸, J. I. Moses⁹, T. K. Greathouse¹⁰, W. Dunn¹¹, R. S. Giles¹, F. Tabataba-Vakili¹, L. N. Fletcher¹², P. G. J. Irwin¹³

¹*MS 183-601, Jet Propulsion Laboratory/California Institute of Technology, 4800 Oak Grove Dr, Pasadena, CA 91109, United States.*

²*Department of Physics and Astronomy, California State University Long Beach, 1250 Bellflower Boulevard, Long Beach, CA 90840, United States.*

³*Planetary Plasma and Atmospheric Research Center, Tohoku University, Aobaku, Sendai, Miyagi 980-8578, Japan.*

⁴*Space Information Center, Hokkaido Information University, 59-2 Nishinopporo, Ebetsu, Hokkaido 069-0832, Japan.*

⁵*Subaru Telescope, National Astronomical Observatory of Japan, 650 North A'ohoku Place, Hilo, HI 96720, United States.*

⁶*National Institute of Information and Communications Technology, 4-2-1, Nukui-Kitamachi, Koganei, Tokyo 184-8795, Japan.*

⁷*Center for Space Physics, Boston University, 725 Commonwealth Ave., Boston MA 02215, United States.*

⁸*Université de Liège, STAR Institute, Laboratoire de Physique Atmosphérique et Planétaire, Quartier Agora B5c, Allée du Six août 19C, B-4000 Liège, Belgium.*

⁹Space Science Institute, 4750 Walnut St #205, Boulder, CO 80301, United States.

¹⁰Southwest Research Institute, 6220 Culebra Rd, San Antonio, TX 78238, United States.

¹¹Department of Space & Climate Physics, University College London, Gower Street, London, WC1E 6BT, United Kingdom.

¹²Department of Physics & Astronomy, University of Leicester, University Road, Leicester LE1 7RH, United Kingdom.

¹³Atmospheric, Oceanic & Planetary Physics, Clarendon Laboratory, University of Oxford, Sherington Road, Oxford OX1 3PU, United Kingdom.

1 **Enhanced mid-infrared emission from CH₄ and other stratospheric hydrocarbons have been**
2 **observed coincident with Jupiter's ultraviolet auroral emission¹⁻³, which demonstrates that**
3 **auroral processes and the neutral stratosphere of Jupiter are coupled. However, the exact**
4 **nature of this coupling has remained an open question. Here, we present a time series of**
5 **Subaru-COMICS images of Jupiter at 7.80 μm measured between January 11-14th, Febru-**
6 **ary 4-5th and May 17-20th (UT) 2017, which show both the morphology and magnitude of**
7 **the auroral CH₄ emission to vary on daily timescales in relation to external solar-wind condi-**
8 **tions. The southern auroral CH₄ emission increased in brightness temperature (T_b) by ΔT_b**
9 **= 3.8 ± 0.9 K between January 11th 15:50 UT - 12th 12:57 UT during a predicted solar-**
10 **wind compression. During the same compression, the northern auroral emission exhibited**
11 **a dusk-side brightening, which mimicks the morphology observed in the ultraviolet auro-**
12 **ral emission during periods of enhanced solar-wind pressures^{4,5}. These results suggest that**
13 **changes in external solar wind conditions perturb the jovian magnetosphere such that ener-**

14 **getic particles are accelerated into the planet’s atmosphere, deposit their energy as deep as**
15 **the neutral stratosphere and modify the thermal structure, abundance of CH₄ or the pop-**
16 **ulation of energy states of CH₄. We also find that the northern and southern auroral CH₄**
17 **emission evolved independently between the January, February and May images, as has been**
18 **observed at X-ray wavelengths over shorter timescales⁶ and at mid-infrared wavelengths over**
19 **longer timescales⁷.**

20 7.80- μm Subaru-COMICS (Cooled Mid-Infrared Camera and Spectrograph) images were
21 obtained from January 11-14th, February 4-5th and May 17-20th 2017 (UT). A subset of images
22 recorded are shown in Figures 1 and 2, which respectively show southern and northern polar pro-
23 jections at times when the southern auroral region (henceforth ‘SAR’, between 330-60°W in Sys-
24 tem III) and northern auroral region (henceforth ‘NAR’, centred at 180°W in system III longitude)
25 were visible on the disk of Jupiter. These images demonstrate variability of both the magnitude
26 and morphology of the 7.80- μm CH₄ emission over timescales of days to months. Further details
27 of the measurements and processing are provided in the Methods and Supplementary sections.

28 In terms of the morphology, the strongest 7.80- μm emission in both auroral regions ap-
29 pears enclosed inside the statistical mean of the ultraviolet emissions of the main oval⁸. Figure 3
30 shows the results of ionosphere-to-magnetosphere mapping model calculations (see Methods) and
31 demonstrates that the positions of strongest CH₄ emission in the auroral regions predominantly cor-
32 respond to radial distances of $>95 R_J$ (beyond the dayside magnetopause⁹ and potentially on open
33 field lines). The exception is the morphology of the emission in the NAR at 16:13 UT on January

34 12th (Figure 2a), when a poleward, duskside feature of stronger emission parallel to the eastern
35 boundary of the statistical oval was observed. This feature was not present less than 24 hours later
36 (Figure 2b) and we have ruled out variable atmospheric seeing conditions between these two nights
37 as the source of this intermittent morphology (see Supplementary Figure 2). A similar morphology
38 of the ultraviolet auroral emission, described as the ‘duskside active region’, has also been observed
39 during periods of enhanced solar-wind pressures and has been attributed to duskside/nightside re-
40 connection associated with the Vasylunas or Dungey cycles or velocity shears caused by changing
41 flows on the nightside magnetospheric flank^{4,5,10}. Indeed, ionosphere-magnetosphere mapping
42 calculations map 73°N, 155°W (an example location covered by the duskside feature) to $\sim 100R_J$
43 at a local time of 19.0 hr. Unlike the NAR, the SAR does not appear to exhibit any smaller-scale
44 morphology although its position at a comparably higher latitude than the NAR does reduce the
45 effective spatial resolution and the ability to resolve smaller-scale features. In contrast to previous
46 studies^{7,11}, we find no obvious movement in the longitudinal position of the southern auroral CH₄
47 emission in the images presented in this work.

48 In order to quantify temporal changes in the magnitude of the auroral emission and its relation
49 to solar-wind conditions, we calculated the residual radiance between each auroral region and a
50 lower-latitude zonal-mean, henceforth named the auroral-quiescent residual (see Methods). Figure
51 4 compares the auroral-quiescent residual and uncertainty for both auroral regions and the results
52 of a solar-wind propagation model (see Methods). The solar-wind propagation model predicts the
53 arrival of a solar-wind compression at Jupiter at approximately 22:00 UT on January 11th, when
54 the dynamical pressure was predicted to have increased from <0.1 nPa to 0.7 nPa. The auroral-

55 quiescent residual increased from $T_b = 8.0 \pm 0.3$ K on January 11th 15:50 UT to 11.8 ± 0.5 K
56 on January 12th 12:57 UT: a net increase of 3.8 ± 0.6 K in T_b or a $\sim 25\%$ increase in radiance.
57 While the viewing geometries of the SAR differ between these two respective images, forward-
58 model calculations of the 7.80- μm emission (see Methods) at these two geometries differ by only
59 0.7 K in T_b and thus cannot explain all of the observed change. From January 12th 12:57 UT to
60 January 14th 12:33 UT, the SAR returned to a similar brightness on January 14th as was observed
61 pre-compression and was a similar brightness in all subsequent measurements (although variability
62 intermediate of these measurements cannot be ruled out).

63 The NAR was not visible on the disk of Jupiter in the images measured on January 11th
64 (before the solar-wind compression) and so we do not know whether it also brightened during the
65 same solar-wind compression. However, the aforementioned duskside-active emission captured by
66 COMICS on January 12th 16:13 UT (Figure 2a) occurred shortly after the solar-wind compression,
67 which reiterates that this morphology is likely driven by enhanced solar-wind conditions and their
68 perturbing effect on the nightside magnetosphere. From January 12th 16:13 UT to January 13th
69 12:30 UT, the auroral-quiescent residual of the NAR was constant in time within uncertainty and
70 subsequently decreased significantly to 1.2 ± 1.1 K. Similarly, measurements in May show the
71 NAR emission to be weak and comparable with, if not weaker, than lower-latitude regions. From
72 May 18th to May 19th, there was a marginal increase in the emission in the NAR during a small
73 ($\Delta p_{dyn} \sim 0.2$ nPa) solar-wind compression however, the change in emission was not significant
74 with respect to measurement uncertainty. Without measurements between the dates of January
75 13th, February 5th and May 18th, it is uncertain whether the NAR emission was consistently

76 weaker in time or whether it exhibited short-term (daily/weekly) variability and the measurements
77 by chance captured periods of weaker emission. However, we favour the latter possibility given that
78 the February-5th and May-17th measurements were preceded by ≥ 7 days of steady, low pressure
79 ($p_{dyn} < 0.05$ nPa) solar-wind conditions. We note the results of a recent study by Kita et al.
80 2016¹⁵, which showed the total auroral power during a solar-wind compression exhibited a positive
81 correlation with the duration of steady, quiescent solar-wind conditions preceding the compression.
82 We also note that the northern auroral C₂H₆ emission weakened during periods of low solar activity
83 in previous work, which similarly suggests a connection with solar-wind conditions on longer
84 timescales¹³.

85 The daily variability of the southern auroral CH₄ emission is suggestive the source of the
86 variability occurs in the upper stratosphere/mesosphere to thermosphere region (10 - 1 μ bar), where
87 the thermal inertial timescales are much shorter (~ 4 weeks at 1 μ bar¹⁴) compared to the lower
88 stratosphere (~ 30 weeks at 1 mbar¹⁴). We suggest the observed changes in CH₄ emission result
89 from either: 1) variable auroral-related heating of the 10- to 1- μ bar level, 2) auroral-driven changes
90 in the vertical profile of CH₄ near its homopause at ~ 1 μ bar, 3) variable non-LTE effects that
91 modify the population of energy states of CH₄ or 4) some combination of 1-3. In order to explore
92 the first two possibilities and determine what magnitude and type of changes in the vertical profiles
93 of temperature or CH₄ could yield a 7.80- μ m $\Delta T_b = 3 - 4$ K increase, we performed a series of
94 radiative-transfer calculations using NEMESIS (see Methods).

95 As shown in Supplementary Figures 5a-b, assuming the CH₄ abundance is held fixed, a 3

96 - 4 K change in T_b would require either: 1) the pressure level of the mesosphere-thermosphere
97 transition to move deeper in the atmosphere by approximately a pressure-scale height or 2) the
98 lapse rate in the thermosphere to increase by a factor of 2. The former corresponds to a total, atmo-
99 spheric temperature increase of more than 100 K at the 0.5- μ bar level, assuming a thermospheric
100 lapse rate similar to that measured during Galileo's descent¹⁵, whereas the latter corresponds to
101 a total, atmospheric temperature increase of ~ 20 K at 0.5 μ bar. In steady state, thermospheric
102 general circulation models show that the mesosphere-thermosphere transition pressure is deeper
103 in the auroral regions compared to non-auroral regions^{16,17}. Yates et al., 2014¹⁸ performed time-
104 dependent thermospheric circulation modelling to investigate the response of the thermospheric
105 structure and circulation to solar-wind compressions and expansion events. Between steady and
106 compressed solar-wind conditions, the model predicted a ~ 20 -K warming and increase in lapse
107 rate at $\sim 70^\circ$ N due to increased rates of joule heating at pressures lower than 1 μ bar (with the lower
108 model boundary set at 2 μ bar). This is consistent with the two-fold increase in thermospheric lapse
109 rate required to brighten the 7.80- μ m emission by $\Delta T_b = 3 - 4$ K, as detailed above.

110 As shown in Supplementary Figure 5c, assuming a fixed vertical temperature profile, in-
111 creasing the altitude of the CH₄ homopause (with respect to the Moses et al., 2005²⁰ Model A CH₄
112 profile) by greater than a pressure-scale height would yield a 3 - 4 K increase in T_b at 7.80- μ m. At
113 the 0.2- μ bar level, this would correspond to a volume mixing ratio (VMR) increase of $\sim 10^{-4}$. In
114 solving the vertical continuity equation assuming the change in VMR is driven entirely by advec-
115 tion and not a chemical source (i.e. $w = (-\Delta X/\Delta t)/(\Delta X/\Delta z)$, where w is the vertical velocity,
116 X is the VMR, t is time and z is height), a change in vertical wind of 2.7 cm s⁻¹ with respect to the

117 steady state would be required. The Bougher et al., 2005 thermospheric model¹⁶ predicts vertical
118 winds at $\sim 70^\circ\text{S}$ of approximately 50 cm s^{-1} at the $0.2\text{-}\mu\text{bar}$ level in steady state and thus a change
119 in vertical wind of 2.7 cm s^{-1} is reasonable. A higher-altitude homopause of CH_4 (and other hy-
120 drocarbons) in Jupiter's auroral regions was also found to optimize the consistency between Juno
121 and Hisaki measurements²⁰.

122 Non-LTE effects are also likely important at the altitudes where the source of variability
123 has been inferred and/or could itself be the driver of the observed variability. In the absence of a
124 strong radiation source, 'classical' non-LTE effects become non-negligible at pressures lower than
125 0.1 mbar , where collisional timescales become longer than the spontaneous radiative lifetime²¹⁻²³.
126 Without a sufficient number of thermal collisions, the population of rotational and vibrational
127 energies deviates from the translational energy population and thus can no longer be described
128 as a Boltzmann distribution. In comparison to non-auroral regions, the upper-stratospheric heating
129 present in Jupiter's auroral regions^{7,19,25} also yields a larger contribution of photons at mid-infrared
130 wavelengths from pressure levels where classical non-LTE processes become non-negligible. In
131 addition, currents of electrons and ions in Jupiter's auroral regions and the resulting charged-
132 particle collisions and dissociative recombinations may induce a non-Boltzmann population of
133 the excited energy states of CH_4 . A further process might be 'H₃⁺-shine', where the downward
134 flux of H₃⁺ emission in lines in the 3- to 4- μm range 'pump' overlapping $\text{CH}_4 \nu_3$ lines, exciting
135 the vibrational modes and thereby modifying the population of lines responsible for the ν_4 band
136 at $\sim 7.80 \mu\text{m}$ ²⁶. Modeling of the aforementioned non-LTE processes will be the subject of future
137 work.

138 We cannot distinguish between temperature, CH₄ abundance, or non-LTE effects in driv-
139 ing the variable CH₄ emission observed between January 11-12th 2017. Nevertheless, either of
140 these processes describes a direct coupling of the neutral stratosphere in Jupiter's auroral regions
141 to the external magnetosphere of Jupiter and solar-wind environment. While daily variability of
142 the northern auroral C₂H₄ and C₂H₆ emission has been observed in previous studies^{27,28}, we be-
143 lieve the results presented in this work represent a significant advance in understanding of this
144 phenomenon. Firstly, the availability of solar-wind measurements and their modelled propagation
145 to Jupiter's orbit allowed the variability of the CH₄ emission to be tentatively linked to exter-
146 nal solar-wind changes and their perturbing effect on the magnetosphere. Secondly, COMICS
147 imaging at high-diffraction limited spatial resolutions have allowed the morphology of the CH₄
148 emission and its variability to be resolved at finer spatial details and mapped to the outer magneto-
149 sphere/magnetopause using ionosphere-to-magnetosphere mapping calculations. Auroral-related
150 heating and chemistry dominate the forcing of the thermal structure and composition at Jupiter's
151 poles^{7,19,25} and the results of this paper suggest these processes are directly connected to the exter-
152 nal magnetosphere. This phenomenon therefore could be ubiquitous for rapidly-rotating Jupiter-
153 like exoplanets with an internal-plasma source around a magnetically-active star²⁹. In particular,
154 MHD (magnetohydrodynamic) simulations of a hot-Jupiter at close orbital separations of 0.05 AU
155 from its host star predict auroral powers of several orders of magnitude larger than on Earth and to
156 affect both polar and equatorial regions³⁰. The coupling of the neutral stratosphere and magneto-
157 sphere of Jupiter presented in this work may therefore be a process of importance in the near-future
158 characterization of Jupiter-like exoplanets from the James Webb Space Telescope and/or directly-

159 imaged planets whose atmospheres are predominantly sensed at higher latitudes.

- 160 1. Caldwell, J., Gillett, F. C. & Tokunaga, A. T. Possible infrared aurorae on Jupiter. *Icarus* **44**,
162 667–675 (1980).
- 163 2. Kim, S. J., Caldwell, J., Rivolo, A. R., Wagener, R. & Orton, G. S. Infrared polar brightening
164 on Jupiter. III - Spectrometry from the Voyager 1 IRIS experiment. *Icarus* **64**, 233–248 (1985).
- 165 3. Flasar, F. M. *et al.* An intense stratospheric jet on Jupiter. *Nature* **427**, 132–135 (2004).
- 166 4. Grodent, D., Gérard, J.-C., Clarke, J. T., Gladstone, G. R. & Waite, J. H. A possible auro-
167 ral signature of a magnetotail reconnection process on Jupiter. *J. Geophys. Res.-Space* **109**,
168 A05201 (2004).
- 169 5. Nichols, J. D. *et al.* Response of Jupiter’s auroras to conditions in the interplanetary medium
170 as measured by the Hubble Space Telescope and Juno. *Geophys. Res. Lett.* **44**, 7643–7652
171 (2017).
- 172 6. Dunn, W. R. *et al.* The independent pulsations of Jupiter’s northern and southern X-ray auro-
173 ras. *Nat. Astr.* **1**, 758–764 (2017).
- 174 7. Sinclair, J. A. *et al.* Independent evolution of stratospheric temperatures in Jupiter’s northern
175 and southern auroral regions from 2014 to 2016. *Geophys. Res. Lett.* **44**, 5345–5354 (2017b).
- 176 8. Bonfond, B. *et al.* The tails of the satellite auroral footprints at Jupiter. *J. Geophys. Res.-Space*
177 **122**, 7985–7996 (2017).

- 178 9. Joy, S. P. *et al.* Probabilistic models of the Jovian magnetopause and bow shock locations. *J.*
179 *Geophys. Res.-Space* **107**, 1309 (2002).
- 180 10. Grodent, D. *et al.* Jupiter's Aurora Observed With HST During Juno Orbits 3 to 7. *J. Geophys.*
181 *Res.-Space* **123**, 3299–3319 (2018).
- 182 11. Drossart, P. *et al.* Thermal profiles in the auroral regions of Jupiter. *J. Geophys. Res.* **98**, 18803
183 (1993).
- 184 12. Kita, H. *et al.* Characteristics of solar wind control on Jovian UV auroral activity deciphered by
185 long-term Hisaki EXCEED observations: Evidence of preconditioning of the magnetosphere?
186 *Geophys. Res. Lett.* **43**, 6790–6798 (2016).
- 187 13. Kostiuk, T. *et al.* P33C-2155: Variability of Mid-Infrared Aurora on Jupiter: 1979 to 2016.
188 In *American Geophysical Union Fall Meeting 2016. P33C: Juno's Exploration of Jupiter and*
189 *the Earth-Based Collaborative Campaign III Posters* (2016).
- 190 14. Zhang, X. *et al.* Radiative forcing of the stratosphere of Jupiter, Part I: Atmospheric cooling
191 rates from Voyager to Cassini. *Planet. Space Sci.* **88**, 3–25 (2013).
- 192 15. Seiff, A. *et al.* Thermal structure of Jupiter's atmosphere near the edge of a 5- μm hot spot in
193 the north equatorial belt. *J. Geophys. Res.* **103**, 22857–22890 (1998).
- 194 16. Bougher, S. W., Waite, J. H., Majeed, T. & Gladstone, G. R. Jupiter Thermospheric Gen-
195 eral Circulation Model (JTGCM): Global structure and dynamics driven by auroral and Joule
196 heating. *J. Geophys. Res.-Planet* **110**, E04008 (2005).

- 197 17. Gérard, J.-C. *et al.* Altitude of Saturn’s aurora and its implications for the characteristic energy
198 of precipitated electrons. *Geophys. Res. Lett.* **36**, L02202 (2009).
- 199 18. Yates, J., Achilleos, N. & Guio, P. Response of the jovian thermosphere to a transient ‘pulse’
200 in solar wind pressure. *Planet. Space Sci.* **91**, 27 – 44 (2014).
- 201 19. Moses, J. I. *et al.* Photochemistry and diffusion in Jupiter’s stratosphere: Constraints from ISO
202 observations and comparisons with other giant planets. *J. Geophys. Res.-Planet* **110**, E08001
203 (2005).
- 204 20. Clark, G. *et al.* Precipitating electron energy flux and characteristic energies in jupiter’s main
205 auroral region as measured by juno/jedi. *J. Geophys. Res.-Space* **123**, 7554–7567 (2018). URL
206 <https://agupubs.onlinelibrary.wiley.com/doi/abs/10.1029/2018JA025639>.
- 207 21. Appleby, J. F. CH₄ nonlocal thermodynamic equilibrium in the atmospheres of the giant
208 planets. *Icarus* **85**, 355–379 (1990).
- 209 22. Kim, S. J. Infrared processes in the Jovian auroral zone. *Icarus* **75**, 399–408 (1988).
- 210 23. López-Puertas, M. & Taylor, F. *Non-LTE Radiative Transfer in the Atmosphere*. Se-
211 ries on atmospheric, oceanic and planetary physics (World Scientific, 2001). URL
212 <https://books.google.com/books?id=1dC9l0q67SYC>.
- 213 24. Sinclair, J. A. *et al.* Jupiter’s auroral-related stratospheric heating and chemistry I: analysis of
214 Voyager-IRIS and Cassini-CIRS spectra. *Icarus* **292**, 182–207 (2017a).

- 215 25. Sinclair, J. A. *et al.* Jupiter’s auroral-related stratospheric heating and chemistry II: analysis
216 of IRTF-TEXES spectra measured in December 2014. *Icarus* **300**, 305–326 (2018).
- 217 26. Halthore, R. N., Allen, J. E., Jr. & Decola, P. L. A non-LTE model for the Jovian methane
218 infrared emissions at high spectral resolution. *Astrophys. J. Lett.* **424**, L61–L64 (1994).
- 219 27. Kostiuk, T., Romani, P., Espenak, F. & Livengood, T. A. Temperature and abundances in the
220 Jovian auroral stratosphere. 2: Ethylene as a probe of the microbar region. *J. Geophys. Res.*
221 **98**, 18823 (1993).
- 222 28. Livengood, T. A., Kostiuk, T. & Espenak, F. Temperature and abundances in the Jovian auroral
223 stratosphere. 1: Ethane as a probe of the millibar region. *J. Geophys. Res.* **98**, 18813 (1993).
- 224 29. Nichols, J. D. & Milan, S. E. Stellar wind-magnetosphere interaction at exoplanets: com-
225 putations of auroral radio powers. *Mon. Not. R. Astron. Soc.* **461**, 2353–2366 (2016).
226 1606.03997.
- 227 30. Cohen, O., Kashyap, V. L., Drake, J. J., Sokolov, I. V. & Gombosi, T. I. The Dynamics of Stel-
228 lar Coronae Harboring Hot Jupiters. II. A Space Weather Event on a Hot Jupiter. *Astrophys.*
229 *J.* **738**, 166 (2011). 1102.4125.

230 **Acknowledgements** All data presented in this work were obtained at the Subaru Telescope, which is
231 operated by the National Astronomical Observatory of Japan (NAOJ). COMICS observations obtained on
232 January 11, 12 and May 19, 20 were proposed by and awarded to co-author YK using Subaru classical time.
233 COMICS observations on January 13, 14, February 4, 5 and May 17, 18 were proposed by and awarded to

234 co-author GSO through the Keck-Subaru time exchange program. We therefore also acknowledge the W. M.
235 Keck Observatory, which is operated as a scientific partnership among the California Institute of Technol-
236 ogy, the University of California and the National Aeronautics and Space Administration and supported by
237 generous financial support of the W. M. Keck Foundation. The authors also wish to recognize and acknowl-
238 edge the very significant cultural role and reverence that the summit of Maunakea has always had within the
239 indigenous Hawaiian community. We are most fortunate to have the opportunity to conduct observations
240 from this mountain. The research was carried out at the Jet Propulsion Laboratory, California Institute of
241 Technology, under a contract with the National Aeronautics and Space Administration. Many thanks to the
242 NASA Postdoctoral and Caltech programs for funding and supporting Sinclair during this research. Orton
243 was supported by grants from NASA to Jet Propulsion Laboratory/California Institute of Technology.

244 **Author contributions** JAS led the analysis of the observations and the preparation of this letter. Co-
245 authors GSO and YK were principal investigators of the awarded telescope time from which the presented
246 data was measured. JAS and co-authors GSO, YK, TMS and TF participated in the measurements at the
247 Subaru telescope. Co-author JF performed the reduction and calibration of the images. Co-authors CT and
248 MFV provided model output, which was invaluable in the interpretation of the results. Co-author PGJI is the
249 lead developer of the NEMESIS code, which was adopted in the paper for radiative transfer forward-model
250 calculations. All remaining authors contributed to the interpretation of the results and the preparation of this
251 publication.

252 **Competing Interests** The authors declare that they have no competing financial interests.

253 **Correspondence** Correspondence and requests for materials should be addressed to author JAS (email:
254 james.sinclair@jpl.nasa.gov).

255 **Methods**

256 **COMICS 7.8- μm images** The COMICS (the COoled Mid-Infrared Camera and Spectrograph^{1,2})
257 instrument is mounted at the Cassegrain focus of the Subaru Telescope, which is located at the
258 Mauna Kea Observatory (approximately 4.2 km above sea level). Subaru's 8.2-metre primary
259 aperture provides a diffraction-limited spatial resolution of $\sim 0.24''$ at 7.8 μm , which corresponds
260 to a latitude-longitude footprint of approximately $2.5^\circ \times 2^\circ$ at $\pm 70^\circ$ in latitude. COMICS provides
261 both imaging and spectroscopic capabilities over a spectral range of approximately 7 to 25 μm .
262 Images are measured on a 320 x 240 array of Si:As BIB (blocked impurity band) pixels each with
263 a scale of $0.13''$, which provides a total field-of-view (FOV) of $42'' \times 32''$. Images can be measured
264 over a number of discrete filters in both the N band (7 to 13 μm) and Q band (17 to 25 μm). In this
265 work, we focus on images obtained in the 7.8- μm filter, which is sensitive to Jupiter's stratospheric
266 CH_4 emission (Supplementary Figure 3). Images were measured on January 11-14, February 4-
267 5 and May 17-20 2017 (UTC). Measurements were performed during periods when Jupiter was
268 available at airmasses lower than 3. The full disk of Jupiter (with equatorial diameters of $\sim 36''$
269 in January, $\sim 39''$ in February and $\sim 42''$ in May) could not be measured in a single image by the
270 COMICS field-of-view (FOV). In January and February measurements, the full disk of Jupiter was
271 measured using a 2 x 1 mosaic of individual images centred at Jupiter's mid-northern and mid-
272 southern latitudes. In May, a 2 x 2 mosaic was conducted due to Jupiter's larger size during this
273 time period. For each individual image, A-frames (of Jupiter) and B-frames (dark sky $60''$ north
274 of Jupiter) were continuously recorded over a total exposure time of 20 seconds. Further details of
275 the measurements presented in this work are provided in Supplementary Table 1.

276 **Imaging processing, calibration and error handling** Images were processed and calibrated us-
277 ing the Data Reduction Manager (DRM). A-B subtraction was performed to remove telluric sky
278 emission. The resulting images were then divided by a ‘bad pixel mask’ accounting for corrupted
279 pixels (due to cosmic ray damage, bright star saturation, manufacturer flaws etc.) and a flatfield in
280 order to remove variations in pixel-to-pixel sensitivity across the detector. A limb-fitting procedure
281 was used to assign latitudes, longitudes and local zenith angles to each pixel on the disk of Jupiter,
282 using the known sub-observer latitude and longitudes at the time of each exposure. The abso-
283 lute radiometric calibration of the images and correction for telluric absorption was conducted by
284 scaling the observed lower-latitude zonal-mean brightness to those measured by Cassini’s CIRS³
285 instrument during the 2001 flyby. This procedure is described in greater detail in Fletcher et al.,
286 2009⁴. We chose this method of calibration since experience with past mid-infrared images of
287 Jupiter and Saturn has demonstrated that the radiometric calibration using a standard star pro-
288 vides inconsistency between datasets obtained on different nights^{4,5}. As detailed further in the
289 ‘Auroral-quiescent residual calculations’ section of Methods, our analysis of the images involved
290 comparing the relative brightness of the auroral regions with a lower-latitude region over time,
291 which negates errors introduced by offsets in the absolute calibration between nights. The reduced
292 and radiometrically-calibrated images are shown in Supplementary Figure 1 in units of brightness
293 temperature (T_b) at 7.80 μm . Portions of the image within 6 pixels (or approximately 0.8”) of
294 the assigned limb were removed as a conservative means of removing the effects of seeing and
295 diffraction in blurring dark sky together with emission from Jupiter. The noise-equivalent spec-
296 tral radiance (NESR) was calculated by finding the standard deviation emission of dark-sky pixels

297 more than $1.5''$ (or approximately 12 pixels) away from the planet. This was calculated for each
298 image to capture changes in sensitivity due to variations in airmass and telluric atmospheric con-
299 ditions between measurements. A centre-to-limb variation correction in the longitudinal direction
300 was applied to correct for the foreshortening and limb-brightening such that longitudes at different
301 viewing geometries on different nights could be more readily compared. A power-law fit, of the
302 form $\log R = a \log \mu + b$, where R is radiance, $\mu = \cos \theta$ and θ is the zenith emission angle, was
303 performed in each latitude band in order to derive a centre-to-limb correction factor. For January
304 and February measurements, we performed the power-law correction using the January 11th 15:50
305 UT image (Supplementary Figure 1a) in the northern hemisphere and the January 13th 12:30 UT
306 image (Supplementary Figure 1d) in the southern hemisphere. For May measurements, the May
307 17th 09:40 UT and May 18 09:35 UT images (Supplementary Figures 1i, j) were similarly chosen
308 to perform the power-law correction in the northern and southern hemispheres, respectively. These
309 specific images were chosen since they best capture non-auroral longitudes in each hemisphere.

310 **Ionosphere to magnetosphere mapping** We adopted the magnetosphere-ionosphere mapping
311 calculation by Vogt et al.^{6,7} to map a location on the planet in planetocentric latitude and sys-
312 tem III longitude to its position in radial distance and local time in the jovian magnetosphere. The
313 calculation is performed by imposing magnetic flux equivalence of a specified region at the equator
314 to the area at which it maps in the ionosphere assuming a given internal field model. For this work,
315 we adopted the VIPAL (Voyager Io Pioneer Anomaly Longitude) internal field model⁸ due to its
316 validity in both the northern and southern hemispheres and to larger ($\sim 95 R_J$) radial distances.
317 Stepping through latitude and longitude in increments of 1° poleward of $\pm 45^\circ$ in latitude, the

318 ionosphere-to-magnetosphere mapping calculation was performed to derive the local time and dis-
319 tance within the magnetosphere at each location. Regions enclosed within the statistical ultraviolet
320 oval for which the calculation did not produce a real value were interpreted as mapping beyond the
321 $95 R_J$ limit of the model, which also marks the estimated position of the dayside magnetopause⁹.
322 This calculation was used to derive the contours of distance shown in Figure 3.

323 **Auroral-quiet residual calculations** Figure 3 demonstrates the areas denoted by ‘Region A’
324 and ‘Region L’ at both high-northern and high-southern latitudes. Region A (for ‘auroral’) was
325 chosen as a sub-region of the auroral regions that mapped to the outer magnetosphere and was
326 commonly sampled by all measurements presented in Figures 1 and 2. Region L was chosen as a
327 lower latitude region away from the area of auroral influence, which is sampled at $\mu = \cos(\theta_{emm})$
328 (where θ_{emm} is the zenith emission angle on Jupiter) in the range $0.4 < \mu < 1$ in each image. By
329 calculating the residual between Region A and Region L, any inconsistencies in the radiometric
330 calibration from one night to the next are effectively removed, which would otherwise affect a
331 comparison of the absolute radiance in time. The mean radiances within Region A and Region L
332 were calculated. The $1-\sigma$ uncertainty on the mean radiance in each region was chosen to be the
333 larger of: 1) the NESR of each image (see Imaging processing, calibration and error handling)
334 scaled by $1/\sqrt{n_p}$ where n_p is the number of pixels averaged or 2) the standard deviation on the
335 mean radiance in the region. The radiances and uncertainties were then converted to brightness-
336 temperature units and the brightness- temperature residual and uncertainty were calculated.

337 **Solar-wind propagation model** The Juno spacecraft continues to provide information on the
338 magnetic and charged particle fields whilst performing 53.5-day orbits inside Jupiter’s magne-

339 tosphere. However, the Juno spacecraft cannot provide *in-situ* measurements of the external solar-
340 wind conditions outside Jupiter’s magnetosphere. In the absence of such measurements, we look
341 instead to modelling results. A solar-wind propagation model¹⁰ was adopted to calculate the solar-
342 wind dynamical pressure ($p_{dyn} = \rho v^2$, where ρ is the density and v is the velocity of the solar wind)
343 impinging on Jupiter’s magnetosphere. This model is used extensively by the outer planets mag-
344 netosphere community^{11–13} in the absence of in-situ measurements of the solar-wind conditions.
345 The model adopts hourly measurements of the solar wind and magnetic field at Earth’s bow-shock
346 nose from OMNI¹⁴ as input and then performs 1-D magnetohydrodynamic (MHD) calculations to
347 model the solar-wind flow out to Jupiter’s bow-shock. The 1-D model prediction of a 3D problem
348 can introduce uncertainties on the arrival time and magnitude of dynamical pressure of solar wind
349 compressions. When the Earth-Sun-Jupiter angle is less than $\pm 50^\circ$, the uncertainty of the arrival
350 time of the solar wind shock is less than ± 20 h and that of the maximum dynamic pressure is
351 38%¹⁵. Given Earth-Sun-Jupiter angles were between $80 - 120^\circ$ in the January-February 2017 time
352 range, we adopted a 48-hour time error on the solar wind propagation model results. In May 2017,
353 the Earth-Sun-Jupiter angle was approximately 18° and thus we assumed a time error of 20 hours
354 in the May time range. These values also appear commensurate with a statistical comparison of
355 1-D MHD predictions and solar-wind data measured by several spacecraft¹⁶. The aforementioned
356 error values are shown in Figure 4 to highlight the potential error to the reader.

357 **Nemesis forward model calculations** A single, broadband measurement of the CH_4 emission
358 does not provide sufficient information to invert or *retrieve* atmospheric parameters and determine
359 at what altitudes they vary. Nevertheless, we computed synthetic or ‘forward-model’ spectra for

360 a range of vertical profiles of temperature and CH₄ in order to explore what changes in those
361 atmospheric parameters could yield the observed, 7.80- μ m, $\Delta T_b = 3 - 4$ K brightening of the
362 southern-auroral region. The NEMESIS forward model and retrieval tool¹⁷ was adopted to com-
363 pute forward-model spectra of the radiance in the COMICS 7.80- μ m bandpass. Forward-model
364 spectra were computed using the line-by-line method using the sources of line information for
365 CH₄, CH₃D and ¹³CH₄, C₂H₂, C₂H₆, NH₃ and PH₃ detailed in Table 4 of Fletcher et al., 2012¹⁸.
366 Calculations were performed using a square instrument function with a width of 0.04 cm⁻¹ (cho-
367 sen based on a balance of a sufficiently high spectral resolution to resolve both weak and strong
368 emission lines whilst minimising computational expense) and subsequently convolved with the
369 COMICS 7.80- μ m bandpass and the telluric transmission spectrum (see Supplementary Figure
370 2). The vertical profiles of temperature and CH₄ were varied as detailed below. The remaining
371 parameters of our model atmosphere, including the vertical profiles of C₂H₂, C₂H₄, C₂H₆, NH₃,
372 PH₃, were held constant since they have negligible effect on the spectrum in the 7.80- μ m band-
373 pass. Further details of the model atmosphere are provided in Sinclair et al., 2017¹⁹. It should be
374 noted that the current NEMESIS forward model assumes local thermodynamic equilibrium (LTE)
375 conditions, whereas, conditions in the auroral regions may have departed from LTE as discussed
376 in the main text.

377 Firstly, we kept the vertical profile of CH₄ and its isotopologues fixed to the ‘model A’ ver-
378 tical profile from Moses et al., 2005²⁰. Starting from the temperature profile shown in Supplemen-
379 tary Figure 4a, we modified the vertical temperature profile in the 0.1-mbar to 1- μ bar range, which
380 includes the transition from the upper stratosphere/mesosphere to the thermosphere. The vertical

381 temperature gradient (or lapse rate) in thermosphere was fixed and the pressure level of the meso-
382 sphere/thermosphere transition was varied as shown in Supplementary Figure 5a. For each profile,
383 a forward model was computed at the same viewing angle ($\mu = \cos(\theta_{emm}) = 0.205$, where θ_{emm} is
384 the emission angle) as Region A in the southern auroral region on January 12th 12:57 UT (during
385 the solar-wind compression). The synthetic spectrum was convolved with the 7.80- μm bandpass
386 (as detailed above) and converted into units of brightness temperature (T_b). These T_b values are
387 shown in the legend in Supplementary Figure 5a. A further set of forward models and brightness
388 temperatures were similarly computed, where the pressure level of the mesosphere/thermosphere
389 transition was fixed at 0.2 μbar and the vertical temperature gradient (or lapse rate) was varied, as
390 shown in Supplementary Figure 5b.

391 Secondly, we fixed the vertical profile of temperature as shown in Supplementary Figure 4a.
392 Starting from the vertical profile of CH_4 derived from model A of Moses et al., 2005²⁰, the pressure
393 level of the methane homopause was varied as shown in Supplementary Figure 5c, a forward-
394 model radiance in the 7.80- μm bandpass calculated and converted into brightness-temperature
395 units. These values are shown as the legend of Supplementary Figure 5c.

396 **Data & Code availability** The COMICS images presented in this work are now publically avail-
397 able on the SMOKA (Subaru Mitaka Okayama-Kiso Archive System, <https://smoka.nao.ac.jp/>)
398 following an 18-month proprietary period since measurement. Reduced and calibrated images may
399 be requested from author JAS with permission of the principal investigator of the awarded telescope
400 time (see Acknowledgements). The Data Reduction Manager is a suite of IDL software designed
401 for reduction and processing of planetary images and is available in compressed format from co-

402 author GSO upon request (glenn.s.orton@jpl.nasa.gov). The ionosphere-to-magnetosphere map-
403 ping calculation is also written in IDL and is available from co-author MFV (mvogt@bu.edu),
404 upon request. Results of the solar wind propagation model in a specific time period may be re-
405 quested from co-author CT (chihiro.tao@nict.go.jp), upon request. The NEMESIS forward model
406 and retrieval tool is written in Fortran and is available as a GitHub repository: a user account for
407 this repository may be requested from co-author PGJI (patrick.irwin@physics.ox.ac.uk).

- 408 1. Kataza, H. *et al.* COMICS: the cooled mid-infrared camera and spectrometer for the Sub-
410 aru telescope. In Iye, M. & Moorwood, A. F. (eds.) *P. Soc. Photo-Opt. Ins.*, vol. 4008 of
411 *Proceedings of SPIE*, 1144–1152 (2000).
- 412 2. Okamoto, Y. K. *et al.* Improved performances and capabilities of the Cooled Mid-Infrared
413 Camera and Spectrometer (COMICS) for the Subaru Telescope. In Iye, M. & Moorwood,
414 A. F. M. (eds.) *P. Soc. Photo-Opt. Ins.*, vol. 4841 of *Proceedings of SPIE*, 169–180 (2003).
- 415 3. Flasar, F. M. *et al.* Exploring the saturn system in the thermal infrared: The composite infrared
416 spectrometer. *Space Sci. Rev.* **115**, 169–297 (2004).
- 417 4. Fletcher, L. N. *et al.* Retrievals of atmospheric variables on the gas giants from ground-based
418 mid-infrared imaging. *Icarus* **200**, 154–175 (2009).
- 419 5. Parrish, P. D. *et al.* Saturn’s atmospheric structure: the intercomparison of Cassini/CIRS-
420 derived temperatures with ground-based determinations. In *AAS/Division for Planetary Sci-*
421 *ences Meeting Abstracts #37*, vol. 37 of *Bulletin of the American Astronomical Society*, 680
422 (2005).

- 423 6. Vogt, M. F. *et al.* Improved mapping of Jupiter's auroral features to magnetospheric sources.
424 *J. Geophys. Res.-Space* **116**, A03220 (2011).
- 425 7. Vogt, M. F. *et al.* Magnetosphere-ionosphere mapping at Jupiter: Quantifying the effects of
426 using different internal field models. *J. Geophys. Res.-Space* **120**, 2584–2599 (2015).
- 427 8. Hess, S. L. G., Bonfond, B., Zarka, P. & Grodent, D. Model of the Jovian magnetic field
428 topology constrained by the Io auroral emissions. *J. Geophys. Res.-Space* **116**, A05217 (2011).
- 429 9. Joy, S. P. *et al.* Probabilistic models of the Jovian magnetopause and bow shock locations. *J.*
430 *Geophys. Res.-Space* **107**, 1309 (2002).
- 431 10. Tao, C., Kataoka, R., Fukunishi, H., Takahashi, Y. & Yokoyama, T. Magnetic field variations
432 in the jovian magnetotail induced by solar wind dynamic pressure enhancements. *J. Geophys.*
433 *Res.-Space* **110** (2005). A11208.
- 434 11. Badman, S. V. *et al.* Weakening of Jupiter's main auroral emission during January 2014.
435 *Geophys. Res. Lett.* **43**, 988–997 (2016).
- 436 12. Kinrade, J. *et al.* An isolated, bright cusp aurora at Saturn. *J. Geophys. Res.-Space* **122**,
437 6121–6138 (2017).
- 438 13. Lamy, L. *et al.* The aurorae of Uranus past equinox. *J. Geophys. Res.-Space* **122**, 3997–4008
439 (2017).
- 440 14. Thatcher, L. J. & Müller, H.-R. Statistical investigation of hourly OMNI solar wind data. *J.*
441 *Geophys. Res.-Space* **116**, A12107 (2011).

- 442 15. Kita, H. *et al.* Characteristics of solar wind control on Jovian UV auroral activity deciphered by
443 long-term Hisaki EXCEED observations: Evidence of preconditioning of the magnetosphere?
444 *Geophys. Res. Lett.* **43**, 6790–6798 (2016).
- 445 16. Zieger, B. & Hansen, K. C. Statistical validation of a solar wind propagation model from 1 to
446 10 AU. *J. Geophys. Res.-Space* **113**, A08107 (2008).
- 447 17. Irwin, P. G. J. *et al.* The NEMESIS planetary atmosphere radiative transfer and retrieval tool.
448 *J. Quant. Spectrosc. RA.* **109**, 1136–1150 (2008).
- 449 18. Fletcher, L. N. *et al.* The origin and evolution of saturn’s 2011-2012 stratospheric vortex.
450 *Icarus* **221**, 560–586 (2012).
- 451 19. Sinclair, J. A. *et al.* Jupiter’s auroral-related stratospheric heating and chemistry I: analysis of
452 Voyager-IRIS and Cassini-CIRS spectra. *Icarus* **292**, 182–207 (2017a).
- 453 20. Moses, J. I. *et al.* Photochemistry and diffusion in Jupiter’s stratosphere: Constraints from ISO
454 observations and comparisons with other giant planets. *J. Geophys. Res.-Planet* **110**, E08001
455 (2005).

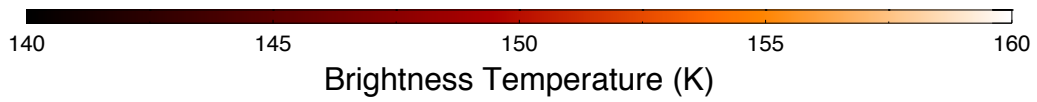
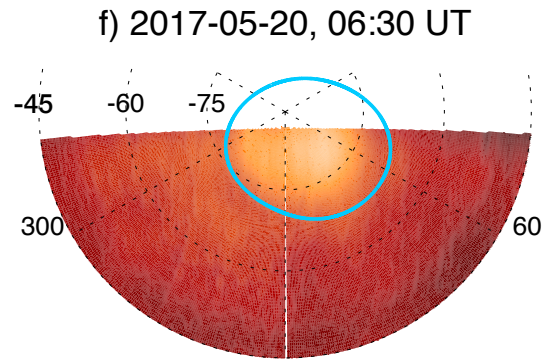
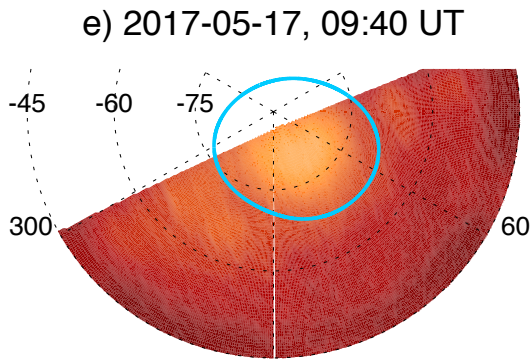
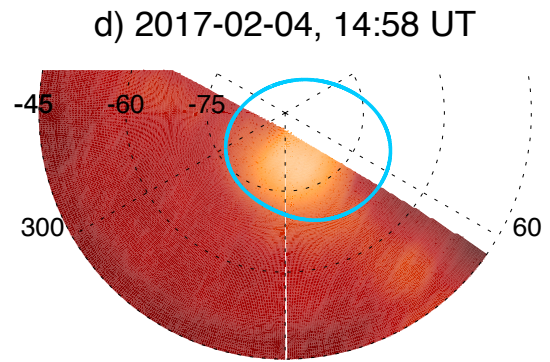
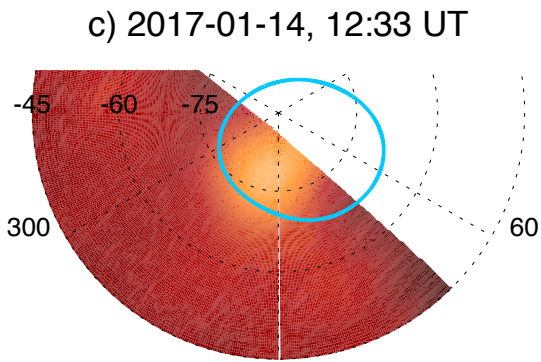
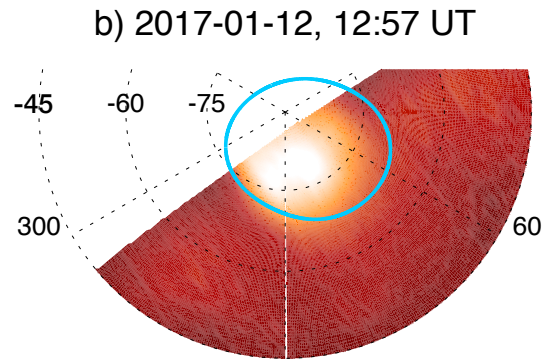
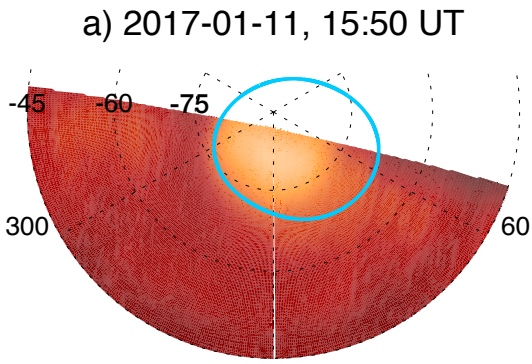
456 **Figure 1** Southern-polar projections of Jupiter's 7.80- μm CH_4 emission. Images were
457 recorded by Subaru-COMICS on (a-c) January 11-14, (d) February 4 and (e-f) May 17,
458 20 2017. These are a subset of the observations shown in Supplementary Figure 1,
459 when the southern auroral region (330-60°W System III) was fully or partially visible on
460 the disk. Images are shown in brightness temperature units according to the bottom
461 colourbar. Solid, light-blue lines represent the statistical-mean position of the ultraviolet
462 auroral main oval emission⁸. For consistency with the Juno science team and the Earth-
463 based community supporting the Juno mission, increasing System III longitude is shown
464 anti-clockwise.

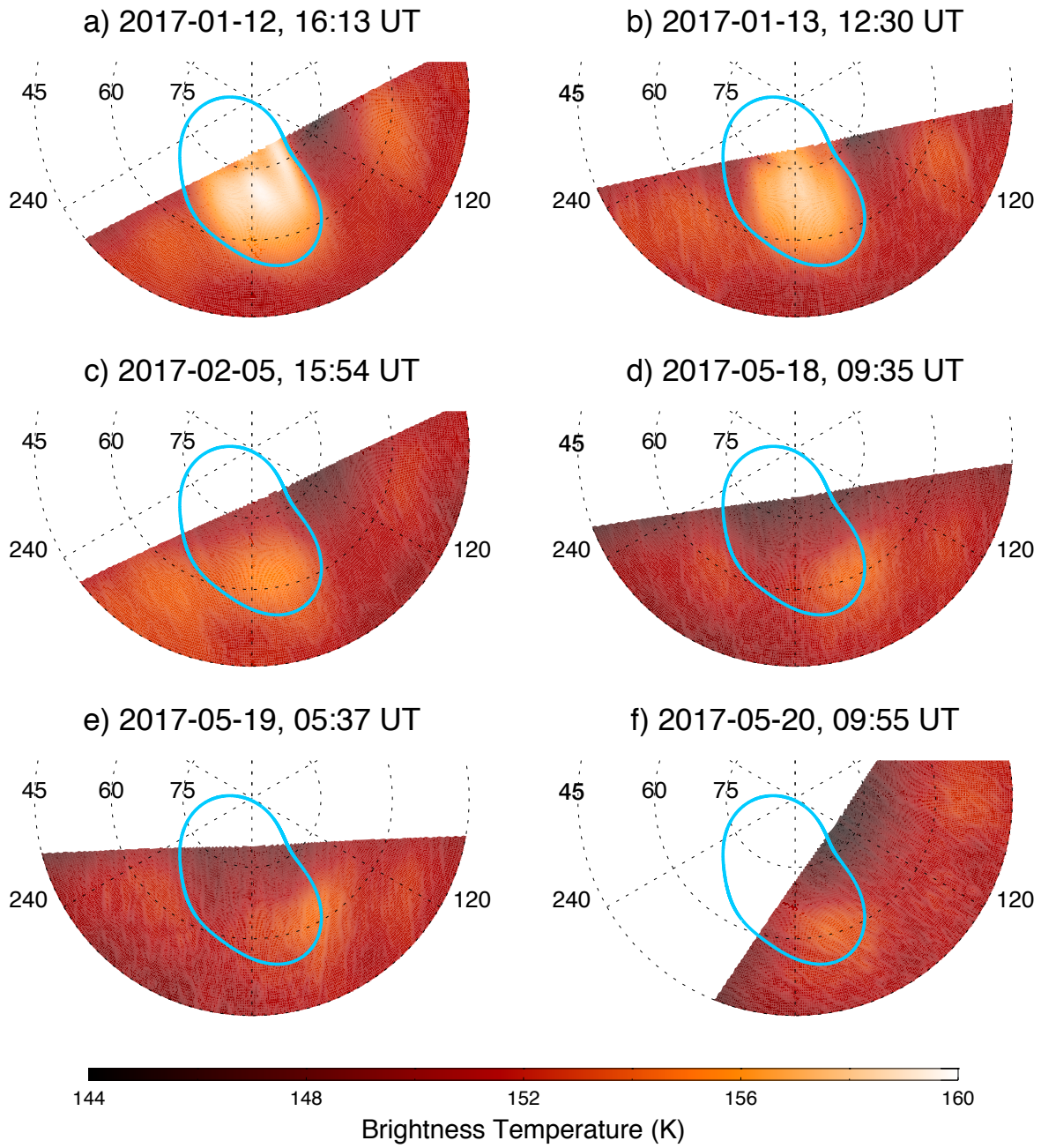
465 **Figure 2** Northern-polar projections of Jupiter's 7.80- μm CH_4 emission. Images were
466 recorded by Subaru-COMICS on (a-b) January 12-13, (c) February 5 and (d-f) May 18-
467 20 2017. These are a subset of the observations shown in Supplementary Figure 1,
468 when the northern auroral region (centred at 180°W, System III) is fully or partially visible
469 on the disk. Images are shown in brightness temperature units according to the bottom
470 colourbar. Solid, light-blue lines represent the statistical-mean position of the ultraviolet
471 auroral main oval emission⁸.

472 **Figure 3** Polar projections and regions chosen for analysis. Subaru-COMICS 7.80- μm
473 images recorded on (a) 2017-01-12 12:57 UT (shown in the south) and (b) 2017-01-13
474 12:30 UT (shown in the north), as in Figures 1 and 2, shown again here for compari-
475 son with the ultraviolet main oval statistical mean⁸ and contours that map to difference

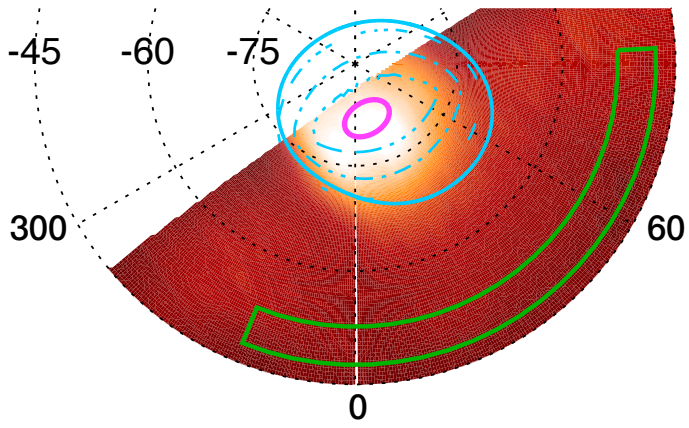
476 distances in the external magnetosphere of Jupiter, as indicated in the legend. The
477 region enclosed within the $95 R_J$ contour is interpreted to map to the outer magneto-
478 sphere/magnetopause. Regions A and L are respectively enclosed within the magenta
479 and green regions and were chosen to represent the auroral and non-auroral regions for
480 calculations of the relative radiance and its variability, as detailed in Methods.

481 **Figure 4** Auroral-quietescent residual brightness-temperature values over time. The resid-
482 ual $7.80\text{-}\mu\text{m}$ brightness temperature between Region A (the auroral region) and Region L
483 (a lower-latitude zonal mean) as described in the text/Methods are shown as red points
484 with error bars. Filled points denote results in the south, unfilled points denote results
485 in the north. Results are shown in a) January 2017 and b) May 2017. Predicted solar-
486 wind dynamical pressures at Jupiter (see Methods) are shown as the solid, black line with
487 horizontal error bars showing the potential time error. The Figure suggests a brightening
488 of Jupiter's southern auroral CH_4 emission in response to a solar-wind compression at
489 approximately 22:00 UT on January 11th 2017.

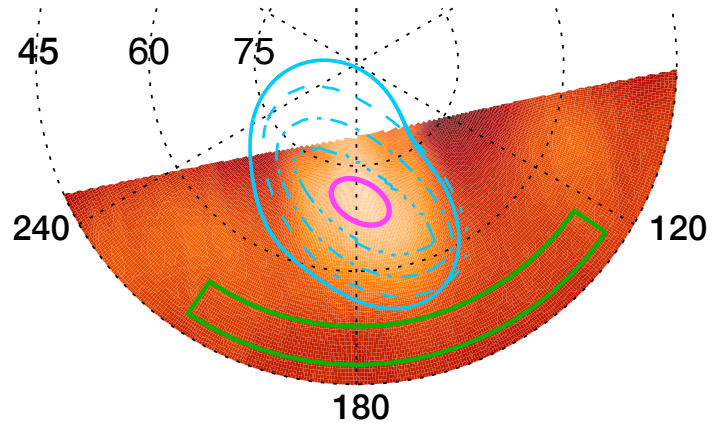




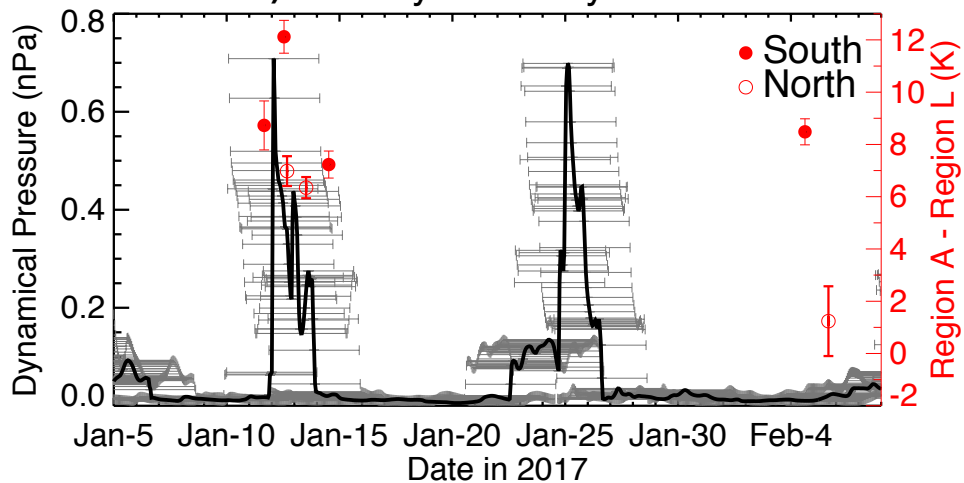
a) 2017-01-12, 12:57 UT



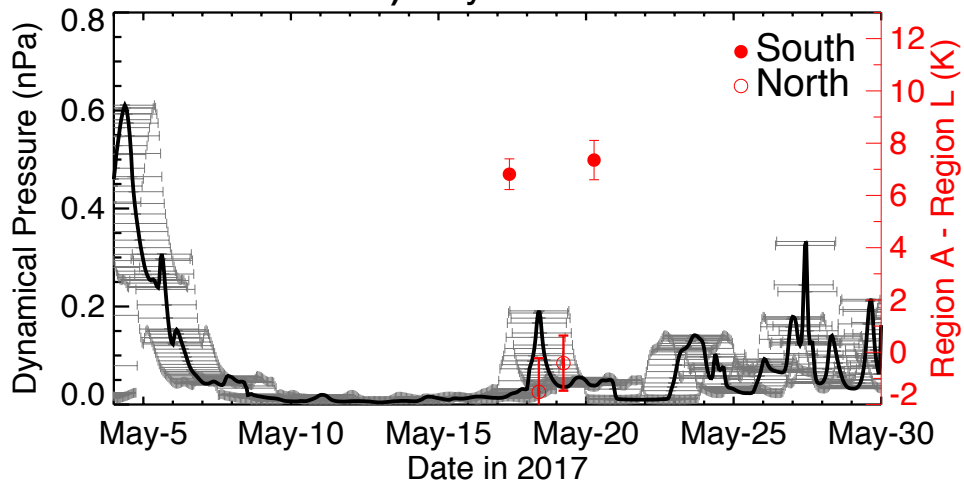
b) 2017-01-13, 12:30 UT



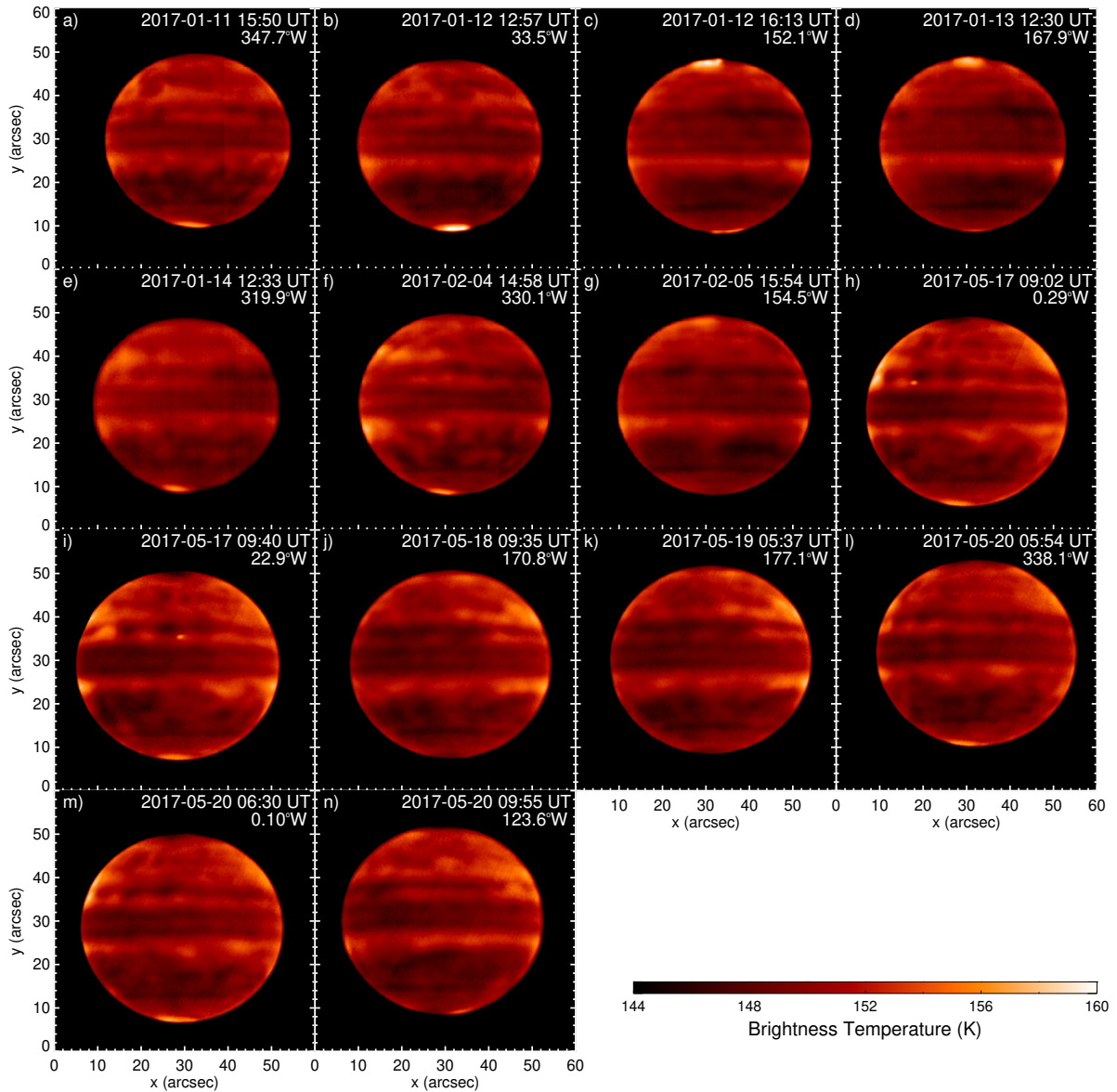
a) January-February 2017



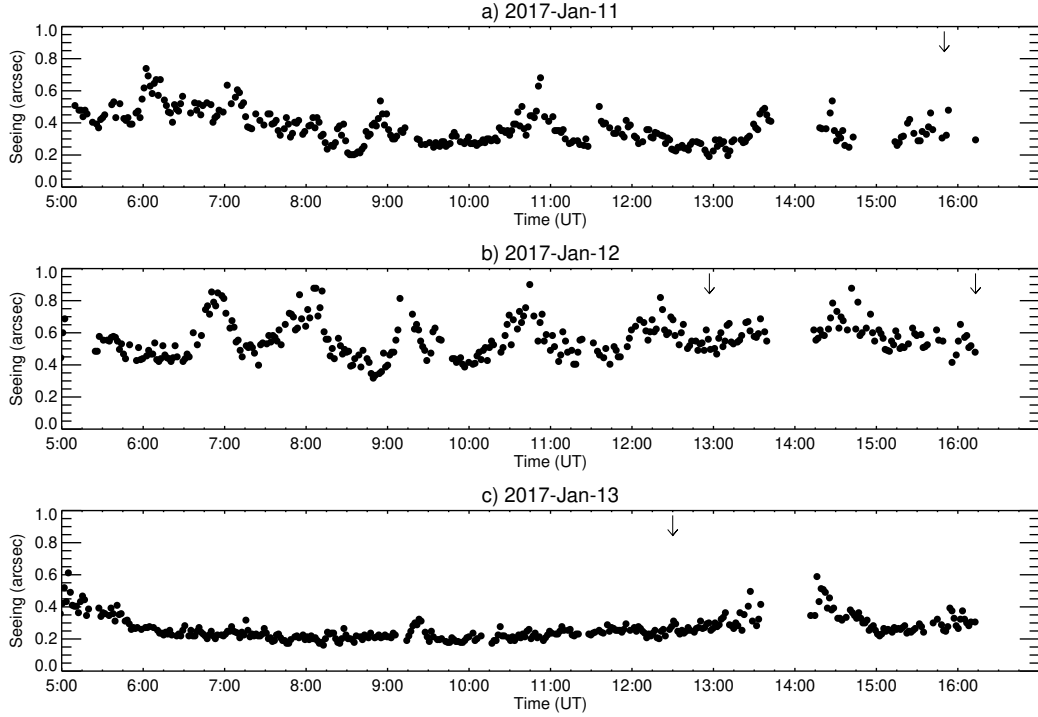
b) May 2017



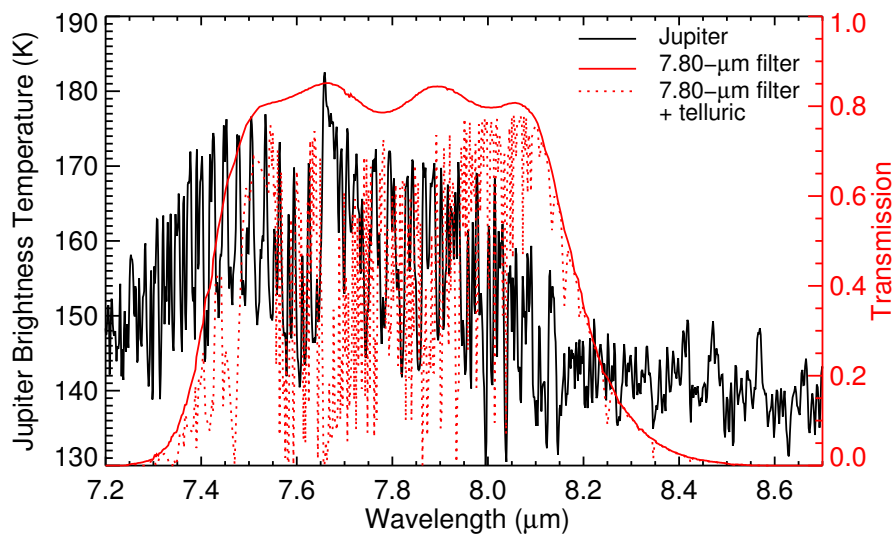
Supplementary information to “A brightening of Jupiter’s auroral 7.8- μm CH₄ emission during a solar-wind compression” by Sinclair et al. 2019.



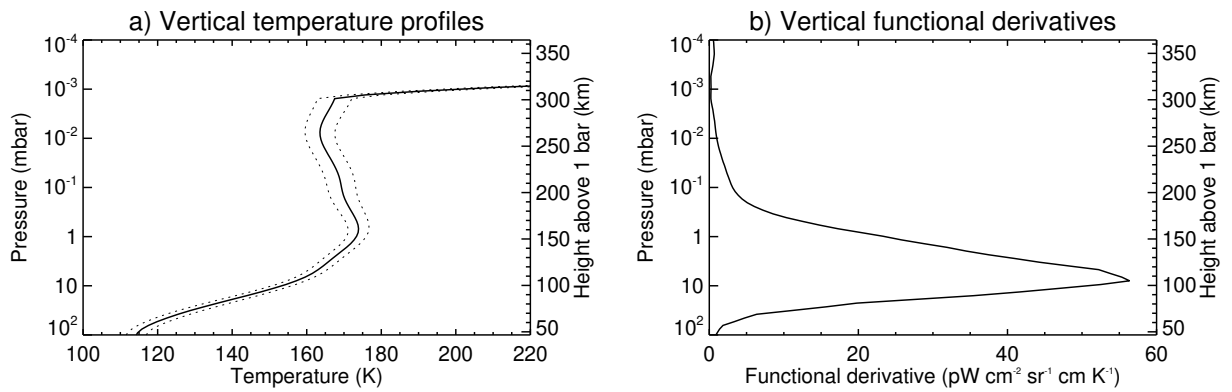
Supplementary Figure 1: Subaru-COMICS images of Jupiter's CH_4 emission. Images are given in chronological order from left-to-right, top-to-bottom and the mean date/time (UTC) and sub-observer System III longitude of each observation are indicated. All images are shown in $7.80\text{-}\mu\text{m}$ brightness-temperature units according to the colourbar at the bottom-right. The bright spot on the disk of Jupiter in panels h) and i) was a Galilean satellite.



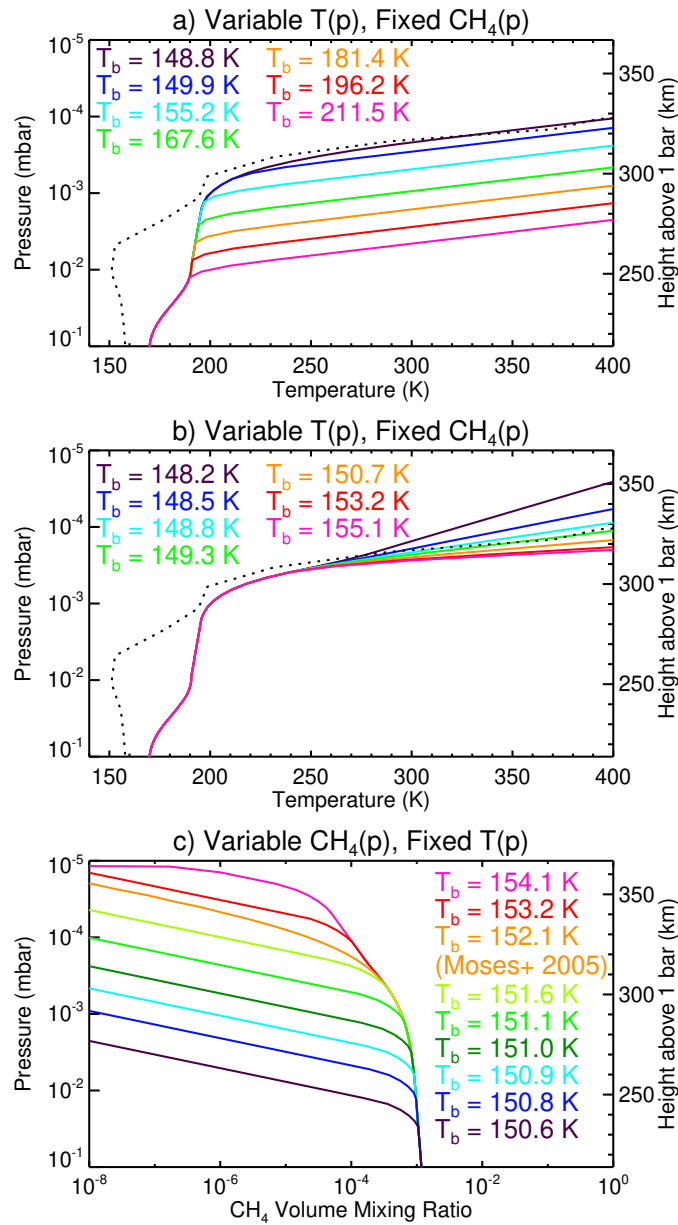
Supplementary Figure 2: Mauna Kea seeing values from January 11-13th. The angular magnitude of seeing (arcsec) at $7.8 \mu\text{m}$ on a) January 11th (UTC), b) January 12th and c) January 13th 2017. The angular magnitude was measured by the Differential Image Motion Monitor (DIMM) taken from the Mauna Kea weather center (mkwc.ifa.hawaii.edu/current/seeing/) at $0.5 \mu\text{m}$ and scaled by a factor of $(0.5/7.8)^{0.2}$ for wavelength dependence. Downward arrows mark the times of a subset of COMICS measurements detailed in Supplementary Table 1. These results demonstrate that atmospheric seeing was poorer on January 12th 16:13 UT compared to January 13th at 12:30 UT ($\sim 0.45''$). Thus, the finer spatial structure observed in the CH_4 emission on January 12th (Figure 2a, main text) and its absence on January 13th (Figure 2b, main text) cannot be explained by poorer seeing on the latter date.



Supplementary Figure 3: The COMICS 7.80- μm bandpass. A brightness temperature spectrum of Jupiter at $\Delta\tilde{\nu} = 0.5 \text{ cm}^{-1}$ (black, solid, of the northern auroral region measured by Cassini-CIRS¹ during the 2001 flyby²), the COMICS 7.80- μm filter response (solid, red) including the telluric transmission spectrum (dotted, red) according to the red right-hand axis.



Supplementary Figure 4: Model temperature profile and functional derivatives. Panel (a) shows the vertical temperature profile (solid) and $1\text{-}\sigma$ uncertainty (dotted) retrieved from IRTF-TEXES (Texas Echelon Cross Echelle Spectrograph on NASA’s Infrared Telescope Facility³) measurements of Jupiter’s northern auroral region (centred at 70°W , 180°W) in December 2014⁴. Panel (b) shows the corresponding vertical functional derivatives with respect to temperature (dR_ν/dT_i , where R_ν is radiance at wavenumber, ν and T_i is temperature at the i^{th} pressure level in the atmosphere). This demonstrates that the $7.8\text{-}\mu\text{m}$ bandpass is predominantly sensitive to CH_4 emission in the 20- to 0.5-mbar range with non-zero sensitivity to pressures as low as 0.1 μbar or ~ 360 km above the 1-bar level.



Supplementary Figure 5: Forward-modelled vertical profiles of temperature and CH_4 . In panel (a), the vertical profile of CH_4 and the lapse rate in the thermosphere were both fixed while the pressure level of the mesosphere-thermosphere transition was varied as shown. In b), the vertical profile of CH_4 and the transition pressure level were fixed while the lapse rate was modified as shown. In panel (c), the vertical profile of temperature was fixed and the height of the CH_4 homopause was modified as shown. The corresponding forward-modelled brightness temperature (T_b) at $7.80 \mu\text{m}$ are indicated by the same colour in the legend of each figure. In panels (a) and (b), the temperature profile measured by Galileo during its descent⁵ is shown as the dotted, black line for comparison.

Supplementary Table 1: Details of the Subaru-COMICS images adopted in this work. All values represent the mean during the exposure time. Dates/times are given in UTC. Negative relative velocities indicate Jupiter moving towards the Earth.

Date (yyyy-mm-dd)	Time (UTC)	Exposure time (s)	Angular diameter (")	Airmass	Relative velocity (km/s)	Filenames
2017-01-11	15:50	20	36.7	1.14	-28.0	wCOMA00134041
						wCOMA00134043
2017-01-12	12:57	20	36.8	1.79	-28.3	wCOMA00134551
	16:13	20	36.8	1.13	-28.0	wCOMA00134553 wCOMA00134843 wCOMA00134845
2017-01-13	12:30	20	36.9	2.09	-28.3	wCOMA00135473 wCOMA00134475
2017-01-14	12:33	20	37.0	2.00	-28.3	wCOMA00136493 wCOMA00136495
2017-02-04	14:58	20	39.4	1.13	-25.9	wCOMA00138283 wCOMA00138285
2017-02-05	15:54	20	39.6	1.18	-25.6	wCOMA00139653 wCOMA00139655
2017-05-17	09:02	20	42.2	1.18	18.19	wCOMA00139989 wCOMA00139991 wCOMA00139993 wCOMA00139995
2017-05-17	09:40	20	42.2	1.29	18.3	wCOMA00140085 wCOMA00140087 wCOMA00140089 wCOMA00140091
2017-05-18	09:35	20	42.1	1.28	18.3	wCOMA00141011 wCOMA00141013 wCOMA00141015 wCOMA00141017
2017-05-19	05:37	20	42.1	1.24	18.3	wCOMA00141385 wCOMA00141387 wCOMA00141389 wCOMA00141391
2017-05-20	05:54	20	42.0	1.18	18.3	wCOMA00142085 wCOMA00142087 wCOMA00142089 wCOMA00142091
2017-05-20	06:30	20	42.0	1.12	18.3	wCOMA00142181 wCOMA00142183 wCOMA00142185 wCOMA00142187
2017-05-20	09:55	20	41.90	1.40	18.3	wCOMA00142675 wCOMA00142677 wCOMA00142679 wCOMA00142681

References

- [1] Kunde, V. G. *et al.* Cassini infrared Fourier spectroscopic investigation. In L. Horn (ed.) *Society of Photo-Optical Instrumentation Engineers (SPIE) Conference Series*, vol. 2803 of *Society of Photo-Optical Instrumentation Engineers (SPIE) Conference Series*, 162–177 (1996).
- [2] Sinclair, J. A. *et al.* Jupiter’s auroral-related stratospheric heating and chemistry I: analysis of Voyager-IRIS and Cassini-CIRS spectra. *Icarus* **292**, 182–207 (2017a).
- [3] Lacy, J. H., Richter, M. J., Greathouse, T. K., Jaffe, D. T. & Zhu, Q. Texas: A sensitive high-resolution grating spectrograph for the mid-infrared. *Publications of the Astronomical Society of the Pacific* **114**, 153–168 (2002). [arXiv:astro-ph/0110521](https://arxiv.org/abs/astro-ph/0110521).
- [4] Sinclair, J. A. *et al.* Jupiter’s auroral-related stratospheric heating and chemistry II: analysis of IRTF-TEXES spectra measured in December 2014. *Icarus* **300**, 305–326 (2018).
- [5] Seiff, A. *et al.* Thermal structure of Jupiter’s atmosphere near the edge of a 5- μm hot spot in the north equatorial belt. *J. Geophys. Res.* **103**, 22857–22890 (1998).